




Immersed boundary simulation of flow through arterial junctions

DWAIPAYAN SARKAR¹, NISHANT UPADHYAY¹, SOMNATH ROY^{2,*} and
SUBHAS CHANDRA RANA¹

¹Department of Mechanical Engineering, National Institute of Technology, Durgapur 713209, India

²Department of Mechanical Engineering, Indian Institute of Technology Patna, Bihta 801103, India
e-mail: dwaipayan.1106@gmail.com; nishantupadhyay9@gmail.com; somnath@iitp.ac.in;
subhasrana@yahoo.co.in

MS received 2 May 2016; revised 4 November 2016; accepted 7 December 2016

Abstract. The present work demonstrates implementation of a mass-conserving sharp-interface immersed boundary for simulation of flows in branched arterial geometries. A simplistic two-dimensional arterial junction is considered to capture the preliminary flow physics in the aortic regions. Numerical solutions are benchmarked against established available experimental PIV results in Ensley *et al* (*Annu. Thorac. Surg.* 68(4):1384–1390, 1999) and numerical predictions in Gilmanov and Sotiropoulos (*J. Comput. Phys.* 207(2):457–492, 2005) and de Zelicourt *et al* (*Comput. Fluids* 38(9):1749–1762, 2009). Simulations are further carried out for pulsated flows and effects of blockages near the junctions (due to stenosis or atherosclerosis). Instabilities in the flow structures near the junction and the resulting changes in the downstream pulsation frequency were observed. These changes account for the physiological heart defects that arise from the poorly working valve (due to blockage), giving rise to chest pain and breathing instability, and can potentially be used as a detection tool for arterial diseases.

Keywords. Immersed boundary; pulsation; arterial junction.

1. Introduction

Complex cardio-vascular flows play an important role in intricate haemodynamic conditions of anatomical geometries inside a human body. The complexity of the flow can be attributed to the fact that atrial valves (both atrium and ventricle) have a three-dimensional convoluted geometry (bicuspid/tricuspid) that includes curving, branching and tapering in different regions. Thus, flows through these regions are pre-dominated by instabilities and differed frequencies. Also the endothelial cells of the ventricular walls (heart muscles) are exposed to high- and low-shear flows during the cardiac cycles (stresses due to systolic and diastolic pressure) of the heart. As a result, unusual haemodynamic activities in regions like carotid arteries, encephalic regions and aneurysms may induce anomalous biological responses. These responses can potentially lead to deposition of bad (LDL) cholesterol (plaque), thereby narrowing the arterial lumen (endothelium: reducing the diameter of the arterial channel), which is considered as a major reason for heart attacks, strokes and other peripheral

vascular diseases (PVDs) in human beings [1]. The majority of deaths in the developed countries result from cardio-vascular diseases [2], most of which are associated with abnormal blood flow through the aortic regions. Detection and quantification of such complex flow phenomena can help in preventive treatment of some of the heart diseases. Various experimental studies [3] have been performed over the years to accurately model the cardio-vascular flow dynamics and predict the risk factor emerging from those regions. Since the course of the flow entirely depends on the anatomical geometry, detailed models of the vivo geometries are required to replicate the actual circulation [3–5]. Recent developments in the magnetic resonance imaging (MRI) technique have paved a way to detail the diagnostic pictures and unique information on the cardio-vascular system [6]. Substantial information collected through MRI could act as an anatomical and morphological input data for CFD simulations of the vivo geometry. To establish CFD as a powerful clinical tool for a particular disease modelling, there is a need to validate its predicted results with detailed available experimental data; otherwise diagnosing with such aid could lead to erroneous treatment. Hence, to establish CFD as an accurate numerical technique for specific arterial flow simulations, it needs to showcase its versatility to model any type of flow diversities in bio-engineering field.

*For correspondence

Over the last few decades CFD has been a successful tool in numerical prediction for many non-deforming engineering problems (like automobile car and air-craft design), by the use of body-fitted grid. However, due to its limitations over moving and deformed (complicated shapes) geometries, a non-boundary-conforming method, named immersed boundary method (IBM), has gained attention in the last few years mostly because of its ability to model any multi-connected anatomical geometry.

Peskin and McQueen [7] had already initiated the work for developing a three-dimensional computational model of blood flow inside a heart using a viscous incompressible fluid using IBM. Subsequently Ghias *et al* [8] directed efforts to simplify the non-body-conforming grid method with further complex immersed boundary methodologies. Experimental PIV works of Ensley *et al* [4] had paved a way towards designing of total cavopulmonary configuration (TCPC) anatomy with improved surgical scenarios resulting in better postoperative outcomes. Also the recent works of Yokoi *et al* [9] on developing a numerical algorithm for simulating flow inside the complex cerebral aneurism and Zelicourt *et al* [10] on 3D unsteady flow simulations of arbitrarily complex cardio-vascular anatomies had gained considerable popularity in the world of biological fluid-mechanics.

1.1 Outline and contribution

The present solution methodology has been demonstrated to conserve mass and eliminate spurious pressure fluctuations, while preserving the simplicity and efficiency of sharp-interface IBM [11]. The present paper demonstrates applicability of solving flows in blocked arteries near a four-way arterial junction using IBM.

The present study has performed complex boundary simulations of the vivo anatomy. The simulations were carried out using an in-house code developed at IIT Patna, on a typical 2D geometry involving multiple inlets and outlets, also having some constrictions (at least $\frac{1}{4}$ of its original diameter) mimicking a diseased artery. The simulations on the 2D geometry took around 24–27 h (computational time) to run the first 1 lakh time step iterations that involved a flow time of 10 s approximately with a step size of 0.0001 s per iteration (in a 2.66 GHz Intel Xeon Processor), which is much less than efforts needed in 3D simulation. The time-averaged flow measurement results have been quantified based on the frequency of the incoming and outgoing flow and the changes in flow field parameters in the junction region. The results were presented to clinically assist the cardiologists for visualising the typical flow features and carry out the right diagnosis. However, it should be noted that the analysis of 3D model is expected to yield better results for a stenotic valve, which is more realistic in a clinical synopsis, which contributes to the scope of future work.

2. Methodology

2.1 Immersed boundary method (IBM)

The term “immersed boundary method” was first coined by Peskin in (1972) [11] to simulate cardiac flow mechanics and associated blood flow pertaining to fluid–structure interaction. The distinguished feature of this method is that the grid lines do not conform to shape of the boundaries and are independent of the movement of the boundaries. In case of a conventional body-fitted grid, the body needs to conform to the actual mesh in which the boundary itself can act as a grid line, thereby simplifying the implementation of the boundary conditions on it. But a change in the shape of the boundary leads to more complex grid generation, which becomes equally tiresome, and can also lead to some issues with grid quality. Grid generation for complex geometries takes high computational time and the overall simulation time also increases as calculation of metric terms in the transformed coordinate is included. But with IBM no such modifications on the body are required and the simulation can be done over the actual curvilinear geometry using a regular fixed Cartesian grid, the only challenge being implementing the boundary conditions in a way that does not affect accuracy and conservation principles. Gilmanov and Sotiropoulos [12] demonstrated accuracy of sharp interface IBM implementation for flow over complex and deformable geometries. Verzicco *et al* [13] showed that for complex turbulent flows, simulation using a body-conformal mesh is usually costlier than IBM simulations.

2.2 Formulation

2.2a Governing equations: The governing equations considered are the mass conservation (continuity) (Eq. (1)) and the Navier–Stokes (momentum equations) (Eq. (2)) for incompressible Newtonian flow:

$$\nabla \cdot \vec{u}^* = 0 \quad (1)$$

$$\frac{\partial \vec{u}^*}{\partial t^*} + \vec{u}^* \cdot \nabla \vec{u}^* = -\nabla p^* + \frac{1}{\text{Re}} \nabla^2 \vec{u}^*. \quad (2)$$

Non-dimensionalization has been done with appropriate scaling to possibly reduce the effect of the flow variables on the resulting flow solution. Solution of the governing equations of the viscous incompressible flow was obtained by pressure-correction-based MAC algorithm (Harlow and Welch, 1965) with CFL-satisfying time stepping, where an overall second-order accuracy of the pressure–velocity correction was maintained.

It should be noted that blood flow inside arteries and veins is highly non-Newtonian in nature. However, this paper assumed a Newtonian behaviour for the sake of

simplicity. We did not report quantitative values of stresses here but focused only on visualizing the flow patterns due to geometrical complexities and inflow perturbations.

2.2b IBM algorithm: The IBM algorithm gives a general flowchart of the process involved in IBM:

(a) generating structured/unstructured Cartesian grids, (b) locating the stationary nodes or moving nodes inside or outside the geometry, (c) identification of the ghost nodes all along the solid boundary (tagging), (d) interpolating the immersed boundary and interposing the variables at the immersed boundary and (e) solving for the regular nodes.

2.2c Tagging: The entire fluid domain was discretized using a fixed Cartesian mesh. The complex artery geometry is further defined as a triangular unstructured mesh generated using GAMBITTM. This is to mention that the basic solver is for computation of three-dimensional flow configurations. Here, a two-dimensional case is considered where the thickness in the third dimension is negligible (only of three-cell dimension). Location of the computational nodes (Cartesian points) with respect to the boundary mesh was identified. Tagging was done to mark the location of all the computational nodes (as per solid nodes and fluid nodes). Dot product of the position vector and the normal vector of the solid nodes is taken along the body. A positive product ensures that the point is outside the body, whereas a negative value indicates that the point is inside the body and for the zero dot product it lies on the body. The ghost nodes, fluid nodes, and solid nodes at the boundary were registered by the tagging procedure:

$$\begin{aligned} \vec{p} \cdot \hat{n} \geq 0 & \text{ then outside or in the body} \\ \vec{p} \cdot \hat{n} < 0 & \text{ then inside the body} \end{aligned}$$

where p is the position vector and n is the normal vector taken along the body.

2.2d Interpolation to satisfy boundary conditions: In the IBM the boundaries do not coincide with nodes. Therefore, it is important to precisely project the boundary conditions on immersed nodes (orange dot) or ghost nodes (red circular) so that the boundary condition is satisfied. This could be served by interpolation (immersed nodes) or extrapolation (ghost nodes) (figure 1). A second-order polynomial function of the normal distance (n) from the solid wall was considered to maintain the overall second-order accuracy of the solution algorithm.

$$F(n) = an^2 + bn + c. \quad (3)$$

At $n = 0$ (i.e., at the boundary), we consider the boundary condition as follows:

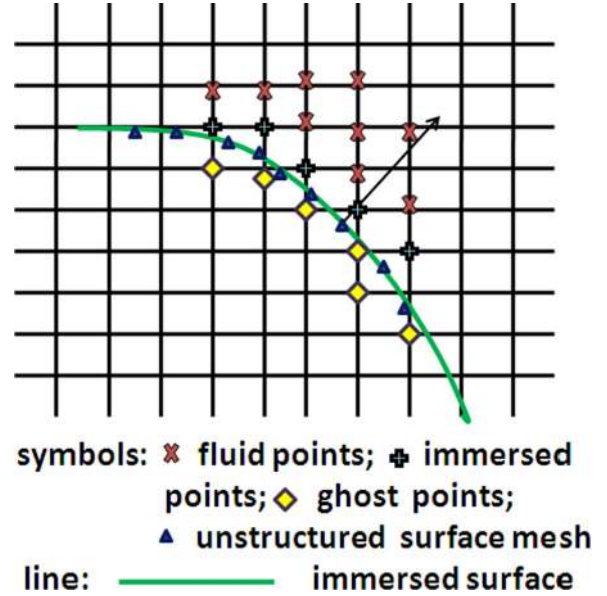


Figure 1. The different tagged points and interpolation direction.

$$\alpha F(0) + \beta F'(0) = \gamma \quad (4)$$

where α and β depend upon nature of boundary condition, i.e., whether it is Dirichlet ($\beta = 0$) or Neumann ($\alpha = 0$) or Robin (mixed for both α and β nonzero) boundary condition. The interpolation was done on the ghost nodes (red) or immersed nodes (orange) using temperature values at regular nodes (green) and the corresponding boundary conditions. The thermal equation is solved for full stencil at regular (green) nodes, and at ghost/immersed node an interpolated value of temperature field is specified in an iterative manner. Intersections of the normal with the first two grid lines (in the solved domain) are considered. The values of the solved variables are interpolated at these two intersection points using the values at the regular nodes and the boundary specification as given by Eq. (4). Hence, three linear equations involving a , b and c (as in Eq. (3)) are obtained and solved to define the interpolation function $F(n)$. A similar quadratic interpolation function has been used for pressure interpolation in incompressible flow solvers with second-order accuracy. The interpolated field variables are further corrected through a SOLA [14] local pressure correction technique. The coupled SOLA–MAC (SOLA for intercepted cells, MAC for fluid cells) implementation preserves the local and global mass conservation in the predicted flow field and also avoids spurious pressure values.

The present IBM methodology has been discussed in detail in a recent publication (Kumar *et al* [15]). It also discusses the accuracy and efficiency of this implementation.

3. Results and discussion

The present methodology was tested over a number of internal flow problems in both 3D and 2D by Kumar *et al* [15]. Problems involving changes in flow and different bends have been investigated and good comparisons with experimental data were reported. In this study, considering the constraints of computational resources we carefully streamlined all flow problems into a realistic time frame, considering a 2D anatomical channel geometry having multiple inlets and multiple outlets. We also considered a non-deforming boundary over time, neglecting systolic and diastolic expansions of the arterial muscles as that would increase the flow complexity over a moving geometry and would need a FSI solver (fluid–structure interaction). The geometry in all cases was treated as a sharp interface solid boundary immersed in a background of Cartesian incompressible fluid domain, which, in this case, was a sufficiently large rectangular box to fully contain the entire geometry under consideration. The junction region had sharp bends resembling a tortoidal tube to capture the flow behaviour occurring in these particular regions. This particular study has been made to (1) validate our 2D immersed boundary formulation with the 3D cardiovascular model of Zelicourt *et al* [10] and experimental data of Ensley *et al* [4], replicating their flow parameters for this particular anatomy and (2) extend our 2D model to simulate the pulsating flow with addition of cholesterol bumps at different flow regimes of the atrial wall.

3.1 Magnified 2D model of arterial geometry—conservation of mass flow rates

This test case presented is an amplified version of the prescribed intra-atrial model with a relatively coarser mesh. It is a simpler version of the more complex scenario just to visualize the distributions of flow at the junction region and check the mass flow rates at different inlets and outlets to ensure mass conservation. All the four channels have the same width (D) and their junction is offset by one channel width. Entrance and exit lengths are spanned $0.75D$ between the boundaries and the closest pipe axis. The flow distributions between the two inlets are considered as per the PIV experimental study conducted by Ensley *et al* [4], in which 60% of the flow enters from right inlet and 40% of the flow from left inlet and the flow is subsequently divided among the two outlets. The Reynolds number of the flow is 3900 based on the channel width (0.4) and mean velocity at left inlet. Uniform flow velocity profile (plug flow) is prescribed at both the inlets as per Zelicourt *et al* [10]. The rectangular Cartesian grid is taken to be 100×100 with a uniform mesh. The surface of the pipe junction geometry is discretized with triangular grids of cell size 0.001. All quantities are normalized with respect to the mean velocity at inlet 2. Streamlines and velocity magnitudes are shown

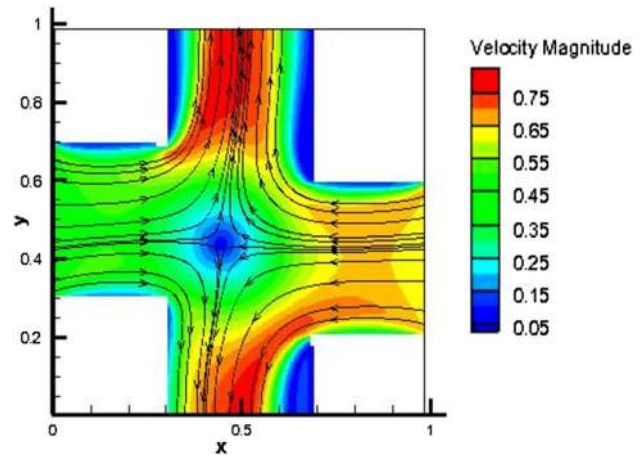


Figure 2. Plot of velocity streamlines showing distribution of flow in the junction region for the afore-mentioned geometry.

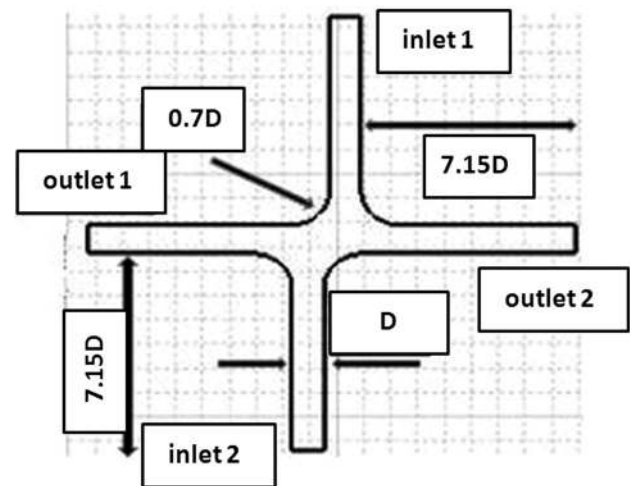


Figure 3. Model of 2D atrial geometry.

over the geometry in figure 2. Calculation of mass flow rates at both the outlet shows a magnitude difference on the order of 0.0184 (less than 2%), which certifies that mass is almost conserved in the present IBM implementation on the boundaries in spite of having superposition of two oppositely directed different flow rates at the junction region.

3.2 Detailed flow features in branched arteries: comparison with reported data

The following case is the two-dimensional idealized representation of the intra-atrial anatomy, which corresponds to the experimental study by Ensley *et al* [4]. Here, we tried to compare our predictions with the experimental observations of Ensley *et al* [4] and 3D CFD study of Zelicourt *et al* [10]. The geometrical considerations are shown in figure 3; entrance and exit lengths are spanned

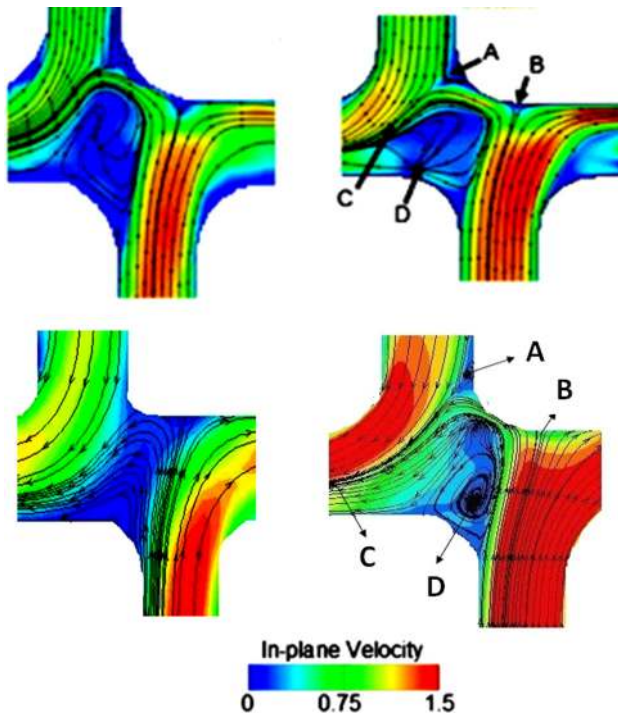


Figure 4. Comparisons between experimental PIV data (top left) and Zelicourt's computational model (top right) of time-averaged velocity with our 2D predictions using coarse mesh (bottom left) and fine mesh (bottom right).

$7.15D$ between the boundaries and the closest pipe axis. Two different Cartesian meshes are considered with two different levels of refinement, (100×100) and (300×300) . The surface of the pipe junction geometry is discretized with a triangular cell size of 0.001 . All other flow conditions and stability criteria remain unchanged. The Reynolds number of the flow based upon the channel diameter is calculated as 1090 as considered in [4] and [13]. It is to be mentioned that though a number of unsteady vortical structures may arise, the flow is well in laminar regime [Zelicourt *et al* 10]. Hence, we present time-averaged data here although no turbulence models have been deployed.

In figure 4, our predictions with coarse and fine meshes have been compared with both experimental and numerical data. It can be seen that the maximum and minimum velocity levels and major flow features predicted at the refined mesh level agree well with previously reported data. Note that the benchmark data of 3D pipe flow cases and the three-dimensional boundary layers impart a narrowing-down effect in the regions of higher velocity. However, good qualitative agreements are observed. Further, the 3D simulation of Zelicourt *et al* [10] identifies important flow features such as (A) separation point, (B) saddle point, (C) merging of the deflected flow near outlet and (D) 3D recirculation zones. Our predictions identify similar features for a 2D representation almost at the same locations. This also substantiates that 2D representation can well

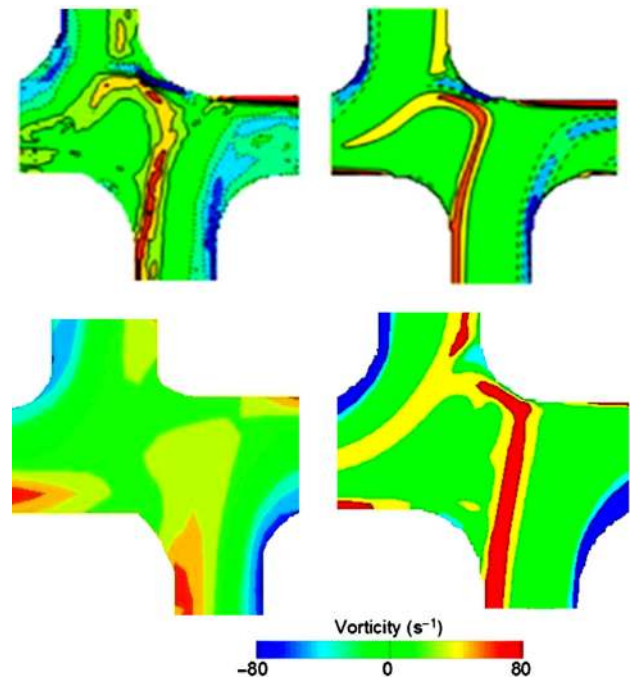


Figure 5. Comparisons of vorticity fields among experimental PIV data (top left), Zelicourt's model (top right) and our 2D predictions using coarse mesh (bottom left) and fine mesh (bottom right).

reproduce important flow features while using a much constrained computational resource.

Figure 5 shows vorticity contours for two different meshes (bottom left—coarse, bottom right—refined) and compares them with experimental and numerical benchmark data. It can be seen that the shear layer is distinctively strong near the left outlet, close to the inlet, with higher mass influx. The high-vorticity shear layer has been well-captured using the present 2D model as its magnitude and distribution agree with experimental data. For all subsequent calculations the refined mesh (i.e., corresponding to 300×300) has been deployed.

The time sequence for vorticity was also analysed. Figure 6 shows the gradual evolution of vorticity shear layers at the junction region at three different instants of time, which also implies that there is an unsteady persistence of shear layers owing to presence of closed conduit and a similar trend tends to be followed with the Zelicourt's unstructured Cartesian immersed boundary (SIIB) method. Importantly, the time scale of the unsteadiness (i.e., existence of big vortex) is 15 s, which is substantial considering the unit diameter and inflow mass flux. Arterial flows are pulsatile in nature and transience can potentially introduce interesting dynamic behaviour. We further use this framework for analysing an arterial flow with more transience and complexities, where optimised codes can be used for real time solutions with 2D approximation.

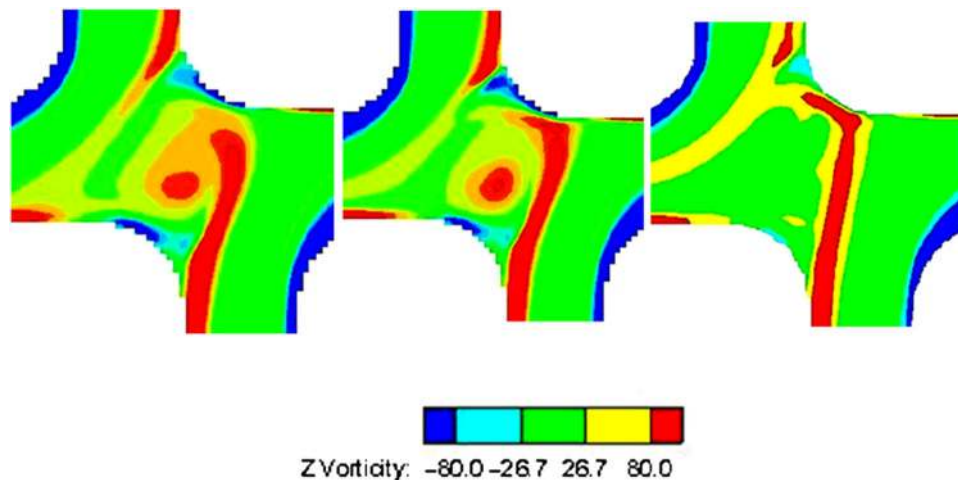


Figure 6. Out-of-plane developing vorticity for the 2D channel geometry at three instants ($t = 1$, $t = 5$, $t = 15$) of time (s).

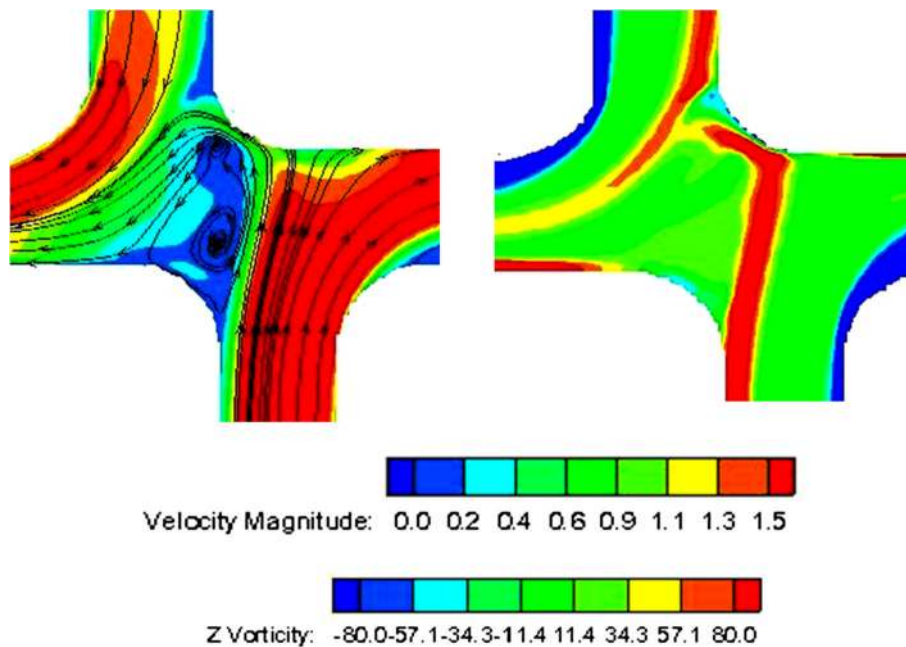


Figure 7. Pulsating velocity and vorticity fields for 90° offset channel.

3.3 Pulsated flow features in branched arteries

Pulsating flow (frequency 72 beats/min) at both the inlets are considered to mimic the pulsed blood flow in arteries. A plot of cycle-averaged velocity and vorticity countours are depicted in figure 7. It can be seen that the peak vorticity zones are substantially stronger as compared with the shear layer for steady inlet shown in figure 6. Velocity signal at the exit is studied for possible dynamic vortex interactions. However, figure 8 shows a sinusoidal behaviour of exit velocities at normal arteries, i.e arteries with no deposition. This indicates that no further transient behaviour is added over

the mean flow features due to inflow pulsation in normal arterial geometries.

3.4 Pulsated flow in arteries with thinning due to cholesterol deposition

Investigations were been further pursued to visualize the complex flow patterns when there is a considerable amount of cholesterol deposition over the arterial walls. These types of deposition in the arterial wall resemble the actual ventricular vessels suffering from “atherosclerosis” or plaque deposition. Further scrutinization has been done to

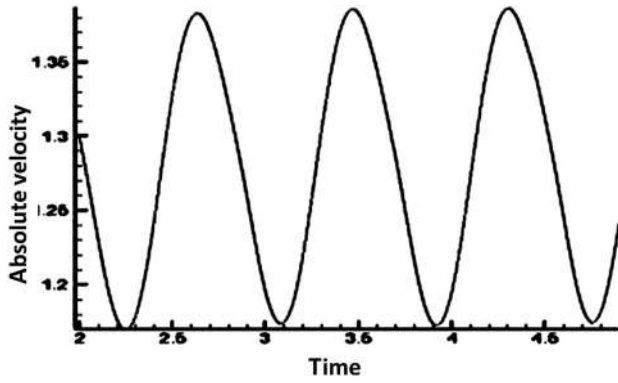


Figure 8. Plot of velocity vs time (s) for a pulsating flow without any deposition.

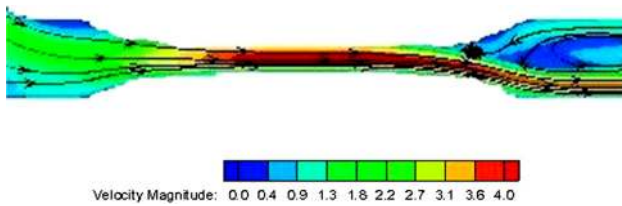


Figure 9. Occurrence of backflow after single cholesterol bump at outlet 2.

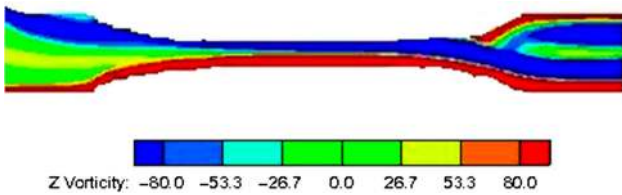


Figure 10. Vorticity fields at the constriction region for single cholesterol deposition.

measure any significant frequency changes occurring in the flow pulse after it passes through the narrow constriction region.

With a single constriction at outlet 2 of the 2D atrial geometry, a high back pressure is formed at the immediate vicinity of the bump end followed by a separation bubble as seen in figure 9. Naturally, a severe backflow is characterized in this region (figure 9), which could create an adverse biological response in the human beings, particularly children. This phenomenon corresponds to insufficiency (also called regurgitation) of flow volume, where the blood that has been pumped outwards leaks back onto the pumping chamber between heartbeats. Also the high extreme vorticity shear layers at the restricted portion (figure 10) could create uneven shear stress on the opposite arterial walls, leading to wear and subsequent rupture of the arterial lumen.

The final focus of this paper was to realize effects of narrowing near the arterial junctions. An arterial anatomy is considered where one inlet (left) and one outlet channel are

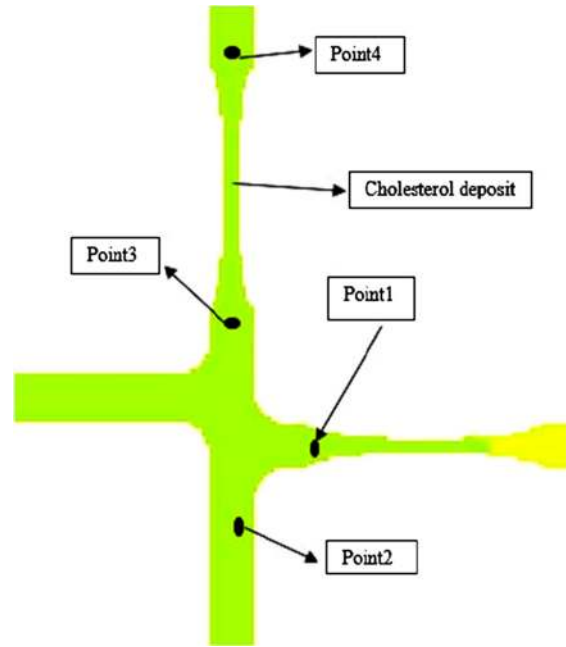


Figure 11. Schematic of the anatomy of a diseased arterial junction.

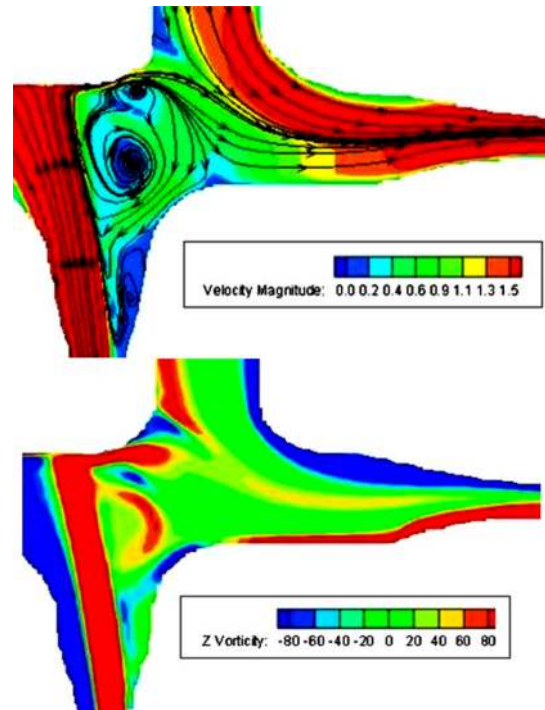


Figure 12. Velocity streamlines and vorticity fields for single uniform deposition at outlet 2.

narrowed by cholesterol deposition. A schematic of the geometry is shown in figure 11. Due to blockage in both inlet and outlet, high erratic intermittent flow behaviour was observed at the intersection of the two channels. Figure 12 shows velocity and vorticity maps (time averaged)

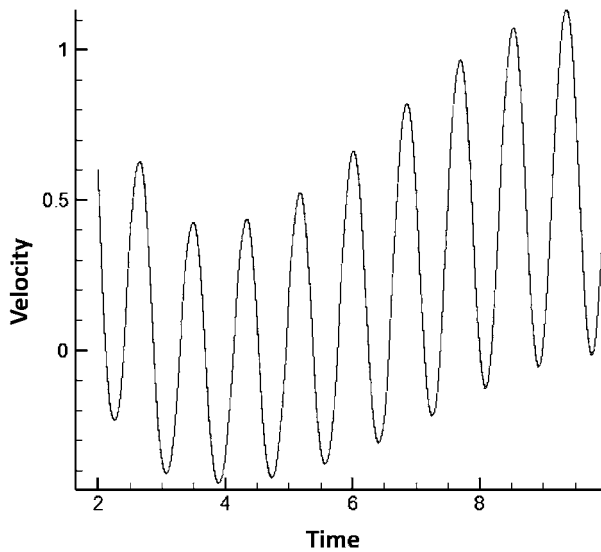


Figure 13. Velocity vs time at point 4 for double-deposition atrial geometry.

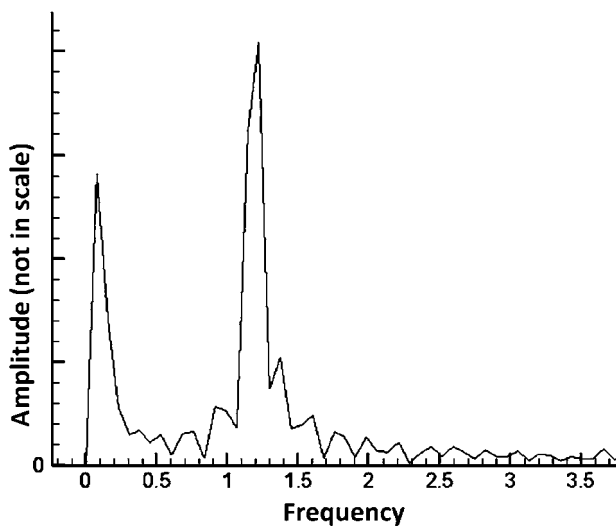


Figure 14. Frequency vs amplitude at point 4 for double deposition on the atrial walls.

in this artery junction, where multiple separation and saddle points can be observed.

The flow field as seen in figure 12 also suggests absolute instability at the junction. In order to confirm the presence of this instability, velocity signal at point 4 (figure 13) is obtained. It is seen that another unsteady frequency has been coupled with inlet perturbation cycle. This increases transience in velocity within the pulmonary artery, which may eventually cause the heart muscles to be dilated. Figure 14 shows FFT of the velocity signal. A low-frequency peak along with the frequency of inlet pulsation is obtained. Therefore, it can be inferred that diseased arteries near the junction show an added instability on top of the pulsation of the inlet flow. Existence of this low frequency in the

velocity signal can be utilized as a diagnostic tool for arterial blockages.

4. Conclusions

This work attempted to simulate the flow patterns in 2D atrial (channel) model. The flow attributes observed in our 2D model had a qualitative consistency with both PIV experimental results and 3D numerical predictions. This validation helped us extend our model to incorporate pulsating flows from both the inlets to contemplate and characterize the difference in flow patterns at various regions of the arterial junction. Further, a number of cholesterol bumps were created at various positions near the arterial junction to find out any range of anomalous behaviour and an erratic response was noted due to the difference in flow frequencies. A perturbation with a frequency of one-sixth of the pulsation rate was detected near the outlet of a blocked arterial branch through an FFT of the velocity signal. This perturbation is due to an absolute instability near the branching as observed in the mean flow visualizations. The measured low frequency value may aid the doctors in detecting a diseased heart suffering from flow obstruction atherosclerosis [16]. The present work can be further augmented for patient-specific geometries obtained through MRI data.

Acknowledgements

We would like to express our thanks to Dr. Manish Kumar, former Ph.D. student (IITP), for his help. Computational resources of IIT Patna and HPC infrastructure have been used.

Nomenclature

| | |
|-------|---------------------------------------|
| D | width of the rectangular channel (mm) |
| p^* | non-dimensional pressure |
| Re | Reynolds number |
| t^* | non-dimensional time |
| u^* | non-dimensional velocity |

References

- [1] HEARTORG/Conditions/CongenitalHeartDefects/AboutCongenitalHeartDefects/Aortic Valve Stenosis, AVS_UCM_307020_Article-www.heart.org
- [2] Mendis S, Puska P and Norrving B 2011 Global atlas on cardio-vascular disease prevention and control. *World Health Organisation in collaboration with World Heart Federation and World Stroke Organisation*, Geneva, Switzerland

- [3] Ku D N 1997 Blood flow in arteries. *Annu. Rev. Fluid Mech.* 1(29): 399–434
- [4] Ensley A E, Lynch P, Chatzimavroudis G P, Lucas C, Sharma S and Yoganathan A P 1999 Towards designing the optimal total cavopulmonary connection: an in vitro study. *Annu. Thorac. Surg.* 68(4): 1384–1390
- [5] Ryu K, Ensley A E, Healy T M, Lucas C, Sharma S and Yoganathan A P 2001 Importance of accurate geometry in the study of the total cavopulmonary connection: computational simulations and in vitro experiments. *Ann. Bio-med. Eng.* 10(29): 844–853
- [6] Svensson J, Gårdhagen R, Heiberg E, Ebbers T, Loyd D, Länne T and Karlsson M 2006 Feasibility of patient specific aortic blood flow CFD simulation. *Medical Image Computing and Computer-Assisted Intervention – MICCAI: 9th International Conference, Copenhagen, Denmark, October 1–6, Proceedings, Part I*
- [7] Peskin C S and McQueen D M 1989 A three-dimensional computational method for blood flow in the heart: 1. Immersed elastic fibres in a viscous incompressible fluid. *J. Comput. Phys.* 81(2): 372–405
- [8] Ghias R, Mittal R and Lund S T A non-body conformal grid method for simulation of compressible flows with complex immersed boundaries. In: *Proceedings of the 42nd AIAA Conference*, 5–8th January 2004
- [9] Yokoi K, Xiao F, Liu H and Fukasaku K 2005 Three-dimensional numerical simulation of flows with complex geometries in a regular Cartesian grid and its application to blood flow in cerebral artery with multiple aneurysms. *J. Comput. Phys.* 1(202): 1–19
- [10] Zelicourt de D, Liang G, Wang C, Sotiropoulos F, Gilmanov A and Yoganathan A 2009 Flow simulations in arbitrarily complex cardio-vascular anatomies—an unstructured Cartesian grid approach. *Comput. Fluids* 38(9): 1749–1762
- [11] Peskin C 1972 *Flow patterns around heart valves: a digital computer method for solving the equations of motion*. Phd Thesis, Albert Einstein College of Medicine, No. 7230378
- [12] Gilmanov A and Sotiropoulos F 2005 A hybrid cartesian/immersed boundary method for simulating flows with 3D, geometrically complex, moving bodies. *J. Comput. Phys.* 207(2): 457–492
- [13] Verzicco R, Mohd-Yusof J, Howarth D and Orlandi P 2000 Large eddy simulation in complex geometry configurations using boundary body forces. *AIAA J.* 38(3): 427–433
- [14] Hirt C W, Nichols B D and Romero N C 1975 *SOLA: a numerical solution algorithm for transient fluid flows*. Technical report LA-5852, Los Alamos Scientific Laboratory
- [15] Kumar M, Roy S and Ali Md S 2016 An efficient immersed boundary method for simulation of flow in curved and moving geometries. *Comput. Fluids* (129): 159–178
- [16] Cary T and Pearce J (2103) Aortic stenosis: pathology, diagnosis, and medical management of nonsurgical patients. *Crit. Care Nurse* 13(2): 58–72